Rotorcraft aeromechanical system bond graph

Résumé long du chapitre 2

Dans ce chapitre, un modèle aéromécanique d'hélicoptère est développé et la forme de sa représentation bond graphs justifiée. Dans un deuxième temps, la validité du modèle est discutée.
Comme présenté dans le premier chapitre, les phénomènes de RPCs aéroélastiques se manifestent à des fréquences comprises entre 2 et 8Hz (Pavel, et al., 2013), (Muscarello, et al., 2015). *Le modèle développé doit donc être suffisamment représentatif du comportement de l'hélicoptère dans cette plage de basses fréquences. Le premier sous-système qui doit être modélisé, au cœur des comportements dynamiques les plus importants de l'hélicoptère, est le sous-système rotor-fuselage. Dans la plage de fréquences de notre intérêt, le fuselage comme les pales du rotor peuvent être considérés comme des solides rigides* (Bielawa, 2006). *En ce qui concerne les degrés de liberté du fuselage, celui-ci peut translater latéralement et verticalement ainsi que changer d'orientation autour de son axe de roulis, voir ces trois degrés de libertés sur la Figure 2-2. Chaque pale du rotor possède également trois degrés de libertés : battement (« flap »), traînée (« lag ») et pas (« pitch), voir la Figure 2-3. De plus, il est supposé que le rotor tourne à vitesse constante ; cette vitesse est notée tout au long du manuscrit Ω. Le type de rotor modélisé correspond à une technologie particulière qui est celle des rotors articulés, voir Figure 2-1. Pour ce type de rotor, un amortisseur, dit de « traînée » (« lag damper ») est installé entre le manchon en pied de pale et le moyeu du rotor, voir Figure 2-1, afin d'atténuer les phénomènes de résonance sol et air* (Krysinski & Malburet, 2011). *Les hypothèses de modélisation proposées ici sont classiques par rapport à ce que l'on peut retrouver dans la littérature et notamment dans* (Donham, 1969), (Takahashi & Friedmann, 1991) *et* (Krysinski & Malburet, 2011). *Afin d'obtenir les équations du mouvement, il est proposé, comme dans* (Chikhaoui, 2013)*, de les représenter à l'aide de bond graphs vectoriels, appelés également multibond graph (MBG). Il existe plusieurs alternatives pour obtenir les équations du mouvement. Il est choisi ici de s'appuyer sur une approche multicorps, particulièrement adaptée à la description de systèmes d'ingénierie. L'approche multicorps consiste à décomposer un système en corps rigides ou flexibles, reliés entre eux par des liaisons et sur lesquels peuvent s'appliquer des forces extérieures de nature quelconque* (Eberhard & Schiehlen, 2006). *Lorsqu'il est choisi de représenter un système mécanique de corps rigides, par une approche multicorps à l'aide des équations de Newton-Euler, à l'aide de coordonnées relatives, un intérêt des MBG apparait. En effet, la représentation en MBG de chacun de ces corps rigides possède une structure graphique identique. Ceci a été démontré pour la première fois dans* (Tiernego & Bos, 1985). *L'intérêt d'avoir à disposition une structure graphique identifiée est que cela permet de construire le*

graphique d'un système mécanique constitué de plusieurs corps rigides sans avoir la nécessité d'écrire la moindre équation et de procéder par 'copier-coller' de cette fameuse structure, voir Figure 2-5. Cet intérêt a été exploité dans un grand nombre de domaines, et notamment afin de modéliser un robot à segments flexibles (Maschke, 1990), *ou encore la marche humaine* (Hernani, Romero, & Jazmati, 2011) *et plus récemment dans notre laboratoire, en application aux hélicoptères, un système rotor-fuselage* (Chikhaoui, 2013) *et un système de suspension d'hélicoptère* (Boudon, 2014). *Etant donné que l'exploitation de la représentation MBG de corps rigides par les équations de Newton-Euler est utilisée dans tous les modèles développés dans ce manuscrit, qu'il s'agisse du couplage rotor-fuselage ou du modèle biomécanique du bras du pilote, il est proposé de redémontrer la forme de la structure du graph, présentée en Figure 2-5. Cette démonstration, voir les équations (1) à (16), n'utilise pas les notations proposées dans* (Tiernego & Bos, 1985), *mais plutôt celles utilisées dans l'approche analytique de* (Lamoureux, 1992).

Avec cette approche, l'obtention des équations du mouvement d'un système complexe est facilitée. Néanmoins, comme souvent en mécanique, plus les équations son faciles à obtenir et plus le modèle mathématique associé est 'compliqué' : ici, non seulement des équations différentielles ordinaires (ODEs) apparaissent mais également des équations différentielles algébriques (DAEs). Ceci est dû à la redondance des coordonnées et aux contraintes entre corps. Sous la forme de DAEs, un système d'équations linéaires ne peut pas être représenté sous forme d'état d'une manière systématique, ce qui limite les possibilités d'analyse d'un tel système et de son utilisation dans une boucle de contrôle actif en temps réels. De plus, dans le cas général où les équations sont non linéaires, des stratégies particulières doivent être employées afin, soit de transformer les DAEs en ODEs, soit d'intégrer directement les DAEs à l'aide d'une méthode numérique adaptée, comme par exemple, Runge-Kutta implicite ou Backward Differences, voir (Cuadrado, Cardenal, & Bayo, 1997), (Pennestri & Vita, 2004), (Mantegazza & Masarati, 2012).

En ce qui concerne la représentation des liaisons entre corps, une librairie est proposée dans (Zeid & Chung, 1992) *et* (Favre, 1997). *Dans notre cas, les deux types de liaisons nécessaires sont les pivots et les rotules, voir Figure 2-6. Les différentes manières d'imposer des contraintes sont présentées Figure 2-7. Une contribution à la représentation en BG de l'enchaînement de trois liaisons pivots est notamment proposée. La structure du graph est présentée Figure 2-9. Celle-ci permet notamment de supprimer trois équations algébriques et donc de faciliter la résolution numérique du système d'équations par une intervention au niveau graphique. Ce type de liaison, avec un enchaînement de trois liaisons pivots est notamment utile lorsqu'il s'agit de représenter la liaison entre chaque pale et le moyeu d'un rotor articulé, voir Figure 2-1, Figure 2-3 et Figure 2-8.*

Une fois le modèle rotor-fuselage mis en place, les efforts extérieurs, et notamment, les efforts aérodynamiques qui s'appliquent sur les pales du rotor doivent être représentés. Ces efforts jouent un rôle central dans le comportement aéroélastique de l'hélicoptère. Etant donné la faible fréquence, à laquelle les phénomènes auxquels nous nous intéressons apparaissent, une hypothèse acceptable est de considérer ces efforts comme quasi-statique et s'appliquant sur une ligne portante le long de l'envergure d'une pale (Bielawa, 2006), *voir Figure 2-10. De plus,* *comme justifié dans* (Dryfoos, Kothmann, & Mayo, 1999)*, la vitesse induite est négligée car sa dynamique est bien plus rapide que celle de notre intérêt. Le même article, précise qu'une approximation du nombre de Lock (définition autour de l'équation (29)) entre 60 et 70% de sa valeur totale permet d'en tenir compte d'une manière acceptable. Etant donné que les pales sont considérées comme rigides à basses fréquences, il n'est pas nécessaire de les discrétiser spatialement. Néanmoins, il est très souvent nécessaire de tenir compte de caractéristiques aérodynamiques différentes le long de l'envergure de la pale, notamment à cause du vrillage de celle-ci ou de leurs géométries spécifiques. Un modèle d'efforts aérodynamiques quasi-statiques s'adaptant aux caractéristiques aérodynamiques variables le long de l'envergure d'une pale est alors proposé, voir équations (23) à (35) et représentation BG Figure 2-11. Le modèle obtenu impose de discrétiser le champ des vitesses le long de l'envergure de la pale, raison pour laquelle la représentation en MBG est constituée de* ***n branches****. Ce modèle permet de plus, de tenir compte de l'éventuelle vitesse d'avancement de l'appareil sans avoir à modifier le graph. En effet, la vitesse des pales par rapport au référentiel galiléen est obtenue à partir de la représentation MBG des équations de Newton-Euler. Ce modèle est considéré comme une contribution.*

Une fois les modèles du sous-système rotor-fuselage et des efforts aérodynamiques assemblés, on obtient un modèle aéromécanique de l'hélicoptère par bond graph, voir Figure 2-15. A l'aide de ce modèle, il est théoriquement possible de simuler différentes phases de vol comme le vol stationnaire ou d'avancement. Afin de s'assurer de la validité du modèle, il serait nécessaire de comparer des résultats de simulation du modèle avec d'autres modèles eux-mêmes valides ou avec des résultats d'essais. Il est néanmoins presque aussi difficile d'apprendre le langage des bond graphs que d'avoir accès à un modèle valide ou des résultats d'essais dans la communauté des hélicoptéristes. En l'absence de ces informations, il est proposé de vérifier la cohérence du modèle aéromécanique proposé en trois étapes.

La première étape consiste à vérifier le comportement du modèle d'efforts aérodynamiques. Pour cela, le comportement d'une pale en battement soumise à des efforts aérodynamiques est étudié. D'un côté, l'équation (36) représente l'équation linéaire en battement. De l'autre, le modèle aéromécanique développé précédemment est simplifié de la manière suivante : les degrés de liberté du fuselage sont supprimés ainsi que le degré de liberté en traînée de chaque pale. On obtient ainsi un rotor, constitué de 4 pales articulées en battement. Une excitation sinusoïdale en pas collectif variant de 0 à 12 Hz est appliquée aux deux modélisations (équation linéaire du battement d'une pale et modèle bond graph simplifié) et reportée sur la Figure 2-17. Afin de s'assurer, que plus le pas de discrétisation du champ des vitesses des pales par rapport au repère galiléen, est grand, plus les résultats convergent. On fait varier ce pas de discrétisation entre 5 et 20 éléments. La table 2 permet également de vérifier que l'effort de portance statique des deux modélisations de rotors sont proches, et de plus en plus proche avec l'augmentation du pas de discrétisation.

La deuxième étape de la validation est légèrement plus ambitieuse car elle vise la comparaison du modèle sur l'axe vertical de l'hélicoptère à des résultats d'essais au sol, Figure 2-18 et Figure 2-19. Le modèle précédent est réutilisé en libérant le degré de liberté vertical du fuselage. Un couple formé d'un ressort et d'un amortisseur linéaires en parallèle est introduit entre le fuselage et le sol, *représentant ainsi raideur et amortissement du train d'atterrissage. Dans l'expérience menée chez Airbus Helicopters, l'hélicoptère est posé au sol, son rotor tourne et il est demandé au pilote d'exercer une commande de pas collectif sinusoïdale d'amplitude constante et d'une fréquence variant entre environ 0 et 10 Hz. En parallèle, l'accélération verticale du fuselage est mesurée, voir Figure 2-18. Ensuite le rapport entre l'amplitude des accélérations du fuselage et de l'accélération du manche de pas collectif est tracé, voir Figure 2-19. La courbe rouge reproduisant les conditions de l'expérience. On peut voir que l'amplitude est étonnamment proche de ce qui a été mesuré expérimentalement, et que la fréquence du pic résonnant sur cet axe n'est décalée que d'un demi-hertz. Ces deux comparaisons permettent ainsi de valider le modèle aéromécanique proposé sur l'axe vertical de l'hélicoptère.*

Un des intérêts majeurs de ce modèle est qu'il permet d'étudier le phénomène de RPC aéroélastique connu sous la terminologie anglaise de 'vertical collective bounce'. Ce phénomène est le résultat du couplage entre le mode vertical du fuselage posé sur son train, avec le mode collectif de battement des pales du rotor, ainsi qu'avec le mouvement du bras gauche du pilote, qui déplace le manche de pas collectif, sous l'effet des vibrations verticales du cockpit. Ce comportement bio-aéroélastique étant le plus étudié dans la littérature, (Mayo, 1989), (Masarati & Quaranta, 2014), (Muscarello, Quaranta, & Masarati, 2014) *et* (Orlita, 2015), *ce manuscrit se concentre de manière complémentaire sur le comportement bio-aéroélastique de l'hélicoptère sur ses axes latéral et de roulis.*

Ainsi, la dernière étape de validation du modèle, consiste à libérer deux degrés de liberté supplémentaires du fuselage : la translation suivant l'axe latéral et la rotation autour de l'axe de roulis. L'axe vertical du fuselage est libre, le train d'atterrissage n'est plus représenté, le pas collectif des pales à l'équilibre est constant et non nul, l'hélicoptère est en vol stationnaire. De plus, chaque pale possède un degré de liberté de plus : celui dit de « traînée », voir Figure 2-3. Malheureusement, aucun résultat d'essais n'était disponible afin de vérifier le comportement autour de cet axe. On peut néanmoins vérifier la cohérence physique du modèle que nous proposons vis-à-vis du principe de Hamilton. Pour cela, il est proposé de comparer le modèle BG avec un modèle obtenu à partir des mêmes hypothèses en utilisant les équations de Lagrange. Celui-ci est développé en Appendix 2. Ceci ne garantit pas la validité du modèle vis-à-vis de l'expérience, mais permet au moins de vérifier que les deux modèles respectent bien la même loi physique. Le modèle obtenu à partir des équations de Lagrange est linéarisé autour de la position d'équilibre, qui est un vol stationnaire. L'équation (A2.2) en Appendix 2 montre que l'axe vertical de l'appareil est, avec les hypothèses choisies ici, découplé des mouvements cycliques de l'appareil. Ceci ne serait certainement pas le cas si le rotor de queue avait été modélisé. Il est donc décidé de supprimer le degré de liberté du fuselage en translation sur son axe vertical. Des balayages d'amplitude constante à une fréquence variable entre 0 et 10 Hz sur le manche de pas cyclique sont effectués sur les deux modèles. Les résultats présentés en Figure 2-26 sont suffisamment satisfaisants pour pouvoir, dans le futur, les confronter à des résultats d'essais en vol.

In this chapter, first the development of a helicopter aeromechanical model using bond graphs is presented. Then its validity is discussed.

2.1. Rotor-airframe model using multibody dynamics

A central coupling to be modeled in rotorcraft dynamics is the rotor-airframe one. This coupling is at the heart of the most classic aeroelastic phenomenon in helicopters such as *ground resonance*, *air resonance* (Krysinski & Malburet, 2011). Many historical analytical models of this coupling can be found in literature in (Takahashi & Friedmann, 1991) and with a minimalistic number of degrees of freedom in (Krysinski & Malburet, 2011). To avoid these phenomena (Donham, 1969), (Krysinski & Malburet, 2011) a damper is introduced in articulated rotor systems around the lag axis between blades and hub to damp the amplitude of blade lag, see Figure 2-3, movement and position the frequency of its oscillations.

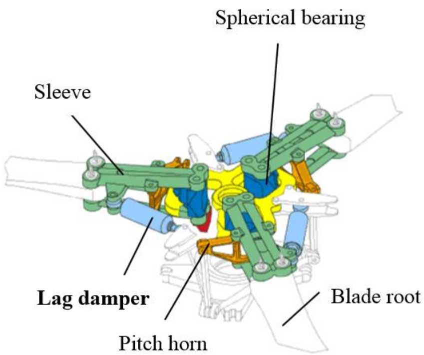

Figure 2-1. Articulated rotor technology

The design of this lag damper is a major concern for rotorcraft designers and it is chosen here to model it with linear characteristics. Since lateral-roll RPCs are known to appear at relatively low frequencies, between 2 and 8Hz (Pavel, et al., 2013), (Muscarello, et al., 2015) the blades and fuselages can be considered as rigid bodies. Modeling them as rigid bodies is an acceptable approximation (Bielawa, 2006) to capture the relevant dynamics at low frequencies, around 3Hz. The fuselage is given 3 degrees of freedom centered on its center of gravity: roll, lateral translation and vertical translation, see Figure 5. Choosing these degrees of freedom allows the center of gravity to have a planar movement, normal to $\mathbf{y}_3$ see Figure 2-2.

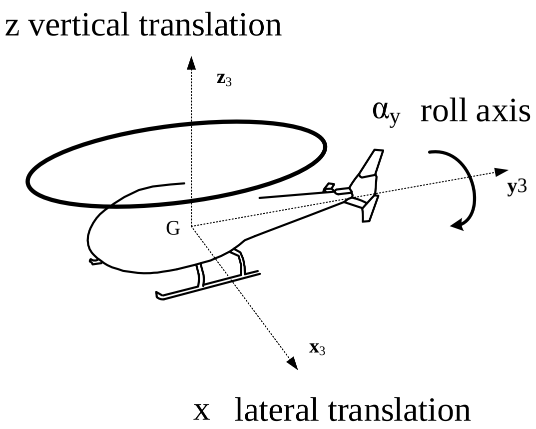

Figure 2-2. Airframe axis definitions

Each blade of the rotor is allowed to flap, lag and pitch see Figure 2-3. In (Pavel, et al., 2013) the flap-lag and blade torsion coupling is mentioned to be modeled when investigating high load maneuvers. It is important to mention too, that during the same high load factor maneuvers, hingeless soft-in plane rotors lag dampers lose their damping and stiffness characteristics decreasing the damping of the flap-lag coupling. In this approach the coupling with blade torsion is however neglected.

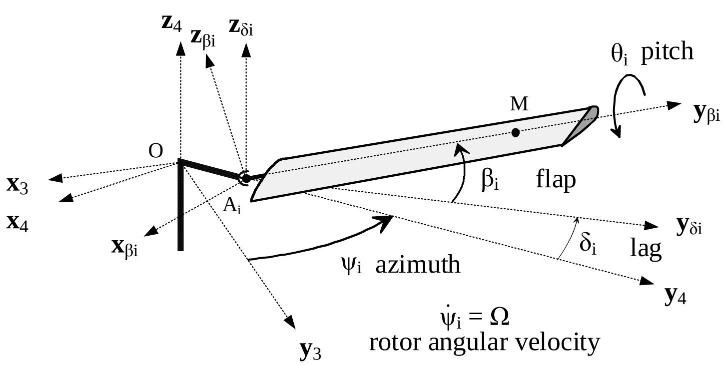

Figure 2-3. Rotor *ith* blade axis definitions

In this section, classic assumptions have been adopted for the mechanical part. In the next, the development of the bond graph to this modeling assumption is presented as well as the aerodynamic model.

2.1.1. Multibody dynamics and Newton-Euler equations in bond graphs

There are many alternatives to derive the equations of motion of systems based on Newton's laws, Hamilton's principle, from which Lagrange equations can be derived or d'Alembert's principle. While in Newton's laws quantities are expressed in terms of vectors (force, momentum, angular momentum) in Lagrangians dynamics the vector quantities are substituted by scalar quantities (energy and work). A major difference between the two formulations results in the choice of coordinates one can make. In the case of Lagrangian dynamics, generalized coordinates of the system are defined globally for the system and eliminate the interaction forces resulting from constraints between elementary parts of the system (Preumont, 2013). When applying Newton laws one has more freedom in the choice of coordinates: each elementary part of the system coordinates' can be chosen as dependent or independent from other elementary parts coordinates'.

Since our interest is on engineering systems, a natural way of describing them is by using multibody dynamics in which the physical system is replaced "*by rigid and or/flexible bodies, joints, gravity, springs, dampers and position and/or force actuators*" (Eberhard & Schiehlen, 2006). The constrained system is then disassembled as free body systems using an appropriate number of inertial, moving reference and body fixed frames for the mathematical description (Eberhard & Schiehlen, 2006). When it comes to the bond graph method a procedure is proposed in (Karnopp D. , 1977), (Favre, 1997) to obtain the bond graph of a multibody system using generalized coordinates. The main drawback of this procedure (Favre, 1997) is that it demands a priori derivation of equations by hand before obtaining the bond graph. Another approach, more systematic (Tiernego & Bos, 1985), (Favre, 1997) in the sense there is no need to identify generalized coordinates or derive a priori any equations by hand is first proposed by (Tiernego & Bos, 1985). It is based on the fact that, when representing a multibody system of rigid bodies using Newton-Euler equations using bond graphs, a pattern appears. It can therefore be reproduced, copied, connected without the need to derive any equation by hand. In this representation the coordinates are *relative* coordinates[10]. The application of this procedure has been used to investigate a flexible robot dynamics (Maschke, 1990), human gait modeling (Hernani, Romero, & Jazmati, 2011), and more recently in our laboratory on helicopter applications: a rotor-airframe system (Chikhaoui, 2013) and a helicopter suspension system (Boudon, 2014).

When modeled with such procedure, the equations of motion can be obtained relatively easily. However, as often in mechanics, the easier the equations of motion are obtained, the more complex the mathematical models are: not only Ordinary Differential Equations (ODE) appear but also Differential Algebraic Equations (DAEs). This is due to the redundancy of coordinates and the implementation of constraints. Under the form of DAEs, a set of linear equations cannot be set in a systematic manner into state-space form, drastically limiting the possibilities to analyze the model or use it in a closed loop for real time calculation. And when the equations are nonlinear, which is the case when dealing with large displacements and

[10] A discussion about the choice of coordinates is out of the scope of this work

complex engineering systems, special strategies have to be used to either transform the DAEs into ODEs or to directly integrate the DAEs with an adapted numerical method such as Backward Differences or Implicit Runge-Kutta, (Cuadrado, Cardenal, & Bayo, 1997), (Pennestri & Vita, 2004), (Mantegazza & Masarati, 2012).
Without being exhaustive about how to model any system using bond graphs for which one can find excellent explanations in (Karnopp, Margolis, & Rosenberg, 2012), (Borutzky, 2009), the modeling of a multibody system in a systematic way is presented following the approach of (Tiernego & Bos, 1985). Using a systematic approach has of course the advantage of being applicable to a large class of problems but the drawback of probably not being the most computationally efficient for a particular problem.

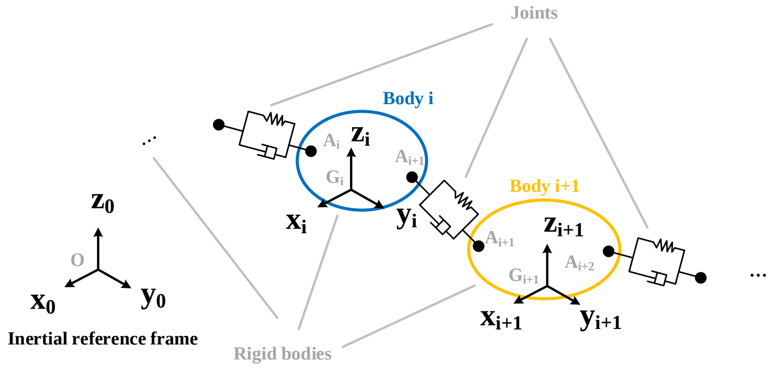

Figure 2-4. A multibody system

To simplify the resulting bond graph from the development of the equations of a multibody system and without loss of generality, one can see on Figure 2-4 that a reference frame has been associated to each rigid body which is chosen to be its principal reference frame and therefore attached to its center of mass.

Step by step, Newton-Euler equations are derived in such a way that efforts and flows of each power bond of the graph become recognizable on Figure 2-5. Let us first isolate the i^{th} body, by definition (Lamoureux, 1992),

$$\sum \mathbf{M}^{i}_{G_i,ext\to i} = {\frac{d}{dt}}^{0} \boldsymbol{\sigma}^{i}_{G_i,i/0} \tag{1}$$

$$\sum \mathbf{F}^{0}_{ext\to i} = m_i {\frac{d}{dt}}^{0} \mathbf{V}^{0}_{G_i,i/0} \tag{2}$$

Now by supposing the body is attached to two bodies, *i-1* and *i+1*, see Figure 2-4,

$$\sum \mathbf{M}^{i}_{G_i,ext\to i} = \mathbf{M}^{i}_{G_i,i-1\to i} + \mathbf{M}^{i}_{G_i,i+1\to i} \tag{3}$$

$$\sum \mathbf{F}^{0}_{ext\to i} = \mathbf{F}^{0}_{i-1\to i} + \mathbf{F}^{0}_{i+1\to i} \tag{4}$$

And decomposing the expressions of the moment of external forces in such a way that the attachment points appear[11],

$$\mathbf{M}^{i}_{G_i,i-1\to i} = \mathbf{M}^{i}_{A_i,i-1\to i} + \mathbf{G}_i\mathbf{A}_i^{\ i} \wedge \mathbf{F}^{i}_{i-1\to i} \tag{5}$$

$$\mathbf{M}^{i}_{G_i,i+1\to i} = \mathbf{M}^{i}_{A_{i+1},i+1\to i} + \mathbf{G}_i\mathbf{A}_{i+1}^{\ i} \wedge \mathbf{F}^{i}_{i+1\to i} \tag{6}$$

By calculating the total time derivative (in the inertial frame) of the angular momentum expressed in the reference frame of the body, two terms can be identified,

$$\begin{aligned}
\frac{d}{dt}^{0}\boldsymbol{\sigma}^{i}_{G_i,i/0} &= \frac{d}{dt}^{i}\boldsymbol{\sigma}^{i}_{G_i,i/0} + \boldsymbol{\Omega}^{i}_{i/0} \wedge \boldsymbol{\sigma}^{i}_{G_i,i/0} \\
&= \frac{d}{dt}^{i}\mathbf{I}_{G,i}\boldsymbol{\Omega}^{i}_{i/0} + \boldsymbol{\Omega}^{i}_{i/0} \wedge \mathbf{I}_{G,i}\boldsymbol{\Omega}^{i}_{i/0} \\
&= \underbrace{\mathbf{I}_{G,i}\frac{d}{dt}^{i}\boldsymbol{\Omega}^{i}_{i/0}}_{\text{inertial element}} + \underbrace{\boldsymbol{\Omega}^{i}_{i/0} \wedge \mathbf{I}_{G,i}\boldsymbol{\Omega}^{i}_{i/0}}_{\substack{\text{Eulerian Junction Structure} \\ \text{MGY element}}}
\end{aligned} \tag{7}$$

It should be noted that $\boldsymbol{I}_{G,i}$ is the inertia matrix of the body around the center of mass of the rigid body expressed in the reference frame of body *i*, that contains the principal axis of the body; the matrix is therefore diagonal.

$$\mathbf{I}_{G,i} = \begin{bmatrix} I_{1,i} & 0 & 0 \\ 0 & I_{2,i} & 0 \\ 0 & 0 & I_{3,i} \end{bmatrix}_{(G,x_i,y_i,z_i)} \tag{8}$$

Concerning the second term that appears, it contains the moments that are generated by gyroscopic effects. This term is responsible for potential precession and nutation motions and plays an important role in the stability of rotor blade and rotor-airframe systems (Bielawa, 2006). The term can be represented in multibond graphs with a modulated multiport gyrator element (MGY) (Borutzky, 2009), which is a power conserving transformation. These moments do not either provide or dissipate energy from the system but result from instantaneous energy transfers (Favre, 1997).

So far, all the efforts of the power junctions of the multibond graph of Figure 2-5 can be determined. In addition, the remaining flows can be determined by expressing the following kinematic relations,

$$\mathbf{V}^{0}_{A_i,i/0} = \mathbf{V}^{0}_{G_i,i/0} + \boldsymbol{\Omega}^{0}_{i/0} \wedge \mathbf{G}_i\mathbf{A}_i^{\ 0} \tag{9}$$

$$\mathbf{V}^{0}_{A_{i+1},i/0} = \mathbf{V}^{0}_{G_i,i/0} + \boldsymbol{\Omega}^{0}_{i/0} \wedge \mathbf{G}_i\mathbf{A}_{i+1}^{\ 0} \tag{10}$$

---

[11] More attachment points could be introduced by adding the necessary expressions as the ones above.

The vectorial products presented above are represented in multibond graphs by a transformation element (TF) that contains the following equation,

$$\begin{aligned}\mathbf{\Omega}^i_{i/0} \wedge \mathbf{G}_i\mathbf{A}_i^{\ i} &= \mathbf{u} \wedge \mathbf{v} \\ &= \begin{pmatrix} a \\ b \\ c \end{pmatrix} \wedge \begin{pmatrix} a' \\ b' \\ c' \end{pmatrix} \\ &= \underbrace{\begin{bmatrix} 0 & c' & -a' \\ -c' & 0 & b' \\ a' & -b' & 0 \end{bmatrix}}_{\mathbf{X}(\mathbf{G}_i\mathbf{A}_i^{\ i})} . \underbrace{\begin{pmatrix} a \\ b \\ c \end{pmatrix}}_{\mathbf{\Omega}^i_{i/0}}\end{aligned} \tag{11}$$

This leads to,

$$\begin{aligned}\begin{pmatrix} effort_{input} \\ flow_{output} \end{pmatrix} &= \begin{pmatrix} \mathbf{G}_i\mathbf{A}_i^{\ i} \wedge \mathbf{F}^i_{i-1\to i} \\ \mathbf{\Omega}^i_{i/0} \wedge \mathbf{G}_i\mathbf{A}_i^{\ i} \end{pmatrix} \\ &= \underbrace{\begin{bmatrix} 0 & \mathbf{X}(\mathbf{G}_i\mathbf{A}_i^{\ i})^T \\ \mathbf{X}(\mathbf{G}_i\mathbf{A}_i^{\ i}) & 0 \end{bmatrix}}_{\text{TF element}} . \underbrace{\begin{pmatrix} \mathbf{\Omega}^i_{i/0} \\ \mathbf{F}^i_{i-1\to i} \end{pmatrix}}_{\begin{pmatrix} flow_{input} \\ effort_{output} \end{pmatrix}}\end{aligned} \tag{12}$$

The projection from the i^{th} body frame to the inertial reference frame demands to multiply by the rotation matrix from the i^{th} reference to the inertial reference and that accounts for all the intermediary body rotations. For any vector $\mathbf{v}^0$ expressed in the inertial reference frame,

$$\mathbf{v}^0 = \mathbf{M}_{i\to 0}.\mathbf{v}^i \tag{13}$$

The expression of the, rotation matrix from the i^{th} reference to the inertial reference frame being,

$$\mathbf{M}_{i\to 0} = \mathbf{M}_{i\to i-1}\mathbf{M}_{i-1\to i-2}...\mathbf{M}_{2\to 1}.\mathbf{M}_{1\to 0} \tag{14}$$

As a result this transformation is state dependent contrarily to the vectorial product presented before, but also power conservative (Karnopp, Margolis, & Rosenberg, 2012). The representation of this transformation using multibond graphs is the following multiport modulated transformer,

$$\begin{pmatrix} effort_{input} \\ flow_{output} \end{pmatrix} = \begin{pmatrix} \mathbf{F}^{i}_{i-1\to i} \\ \mathbf{\Omega}^{0}_{i/0} \end{pmatrix} = \underbrace{\begin{bmatrix} 0 & \mathbf{M}_{i\to 0}{}^{T} \\ \mathbf{M}_{i\to 0} & 0 \end{bmatrix}}_{\text{MTF element}} . \underbrace{\begin{pmatrix} \mathbf{\Omega}^{i}_{i/0} \\ \mathbf{F}^{0}_{i-1\to i} \end{pmatrix}}_{\begin{pmatrix} flow_{input} \\ effort_{output} \end{pmatrix}} \tag{15}$$

Finally, in Figure 2-5, by multiplying each effort by each flow the power that is being transported by each bond can be expressed. What it is proposed on Figure 2-5 differs from (Tiernego & Bos, 1985) in the positioning of the modulated transformer elements: usually only one element is considered by positioning it just above the bottom one junction. This choice facilitates the implementation of additional external forces in the inertial reference which is critical is our application when implementing muscle forces see 3.3.

Furthermore, the sum of the integration of these quantities at the root of the two inertial elements gives the expression of the kinetic energy T_i that is stored in each rigid body at a time t, which is exactly what would be obtained analytically (Lamoureux, 1992) by definition of the kinetic energy of a rigid body in spatial motion,

$$T_i = \frac{1}{2} m_i \mathbf{V}^{0}_{G_i,i/0}{}^{T} . \mathbf{V}^{0}_{G_i,i/0} + \frac{1}{2} \mathbf{\Omega}^{i}_{i/0}{}^{T} . \mathbf{I}_{G,i} . \mathbf{\Omega}^{i}_{i/0} \tag{16}$$

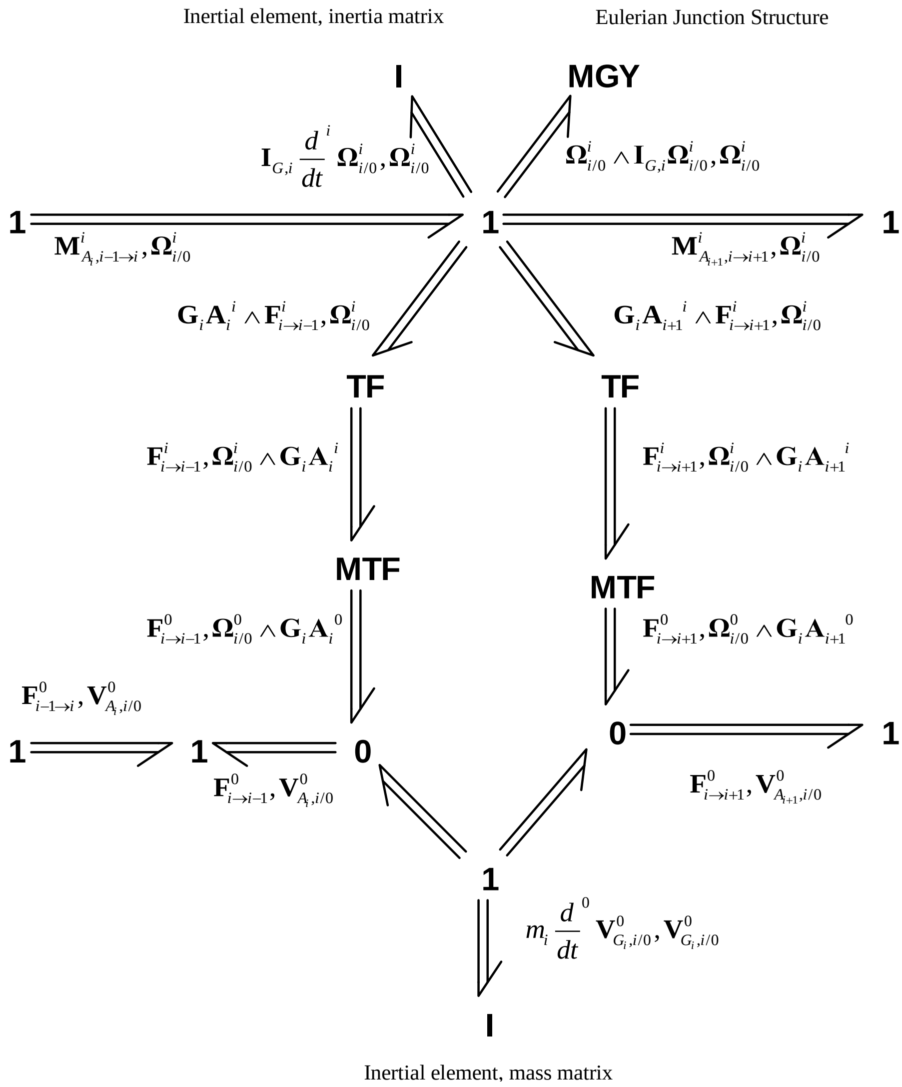

Figure 2-5. Multibond graph of the *i^th^* rigid body spatial motion (effort, flow) at each bond

In order to constrain the motion between bodies, a library of joints using multibond graphs can be found in (Zeid & Chung, 1992) and (Favre, 1997). In this work, the modeling of the rotorcraft and pilot subsystems require to be able to model revolute and spherical joints. The modeling of these two joints is presented by illustrating the three main methods available in literature. On Figure 2-6, the structure of the joint between *i* and *i+1* bodies is presented; the power inputs of this graph are the power outputs of the graph on Figure 2-5.

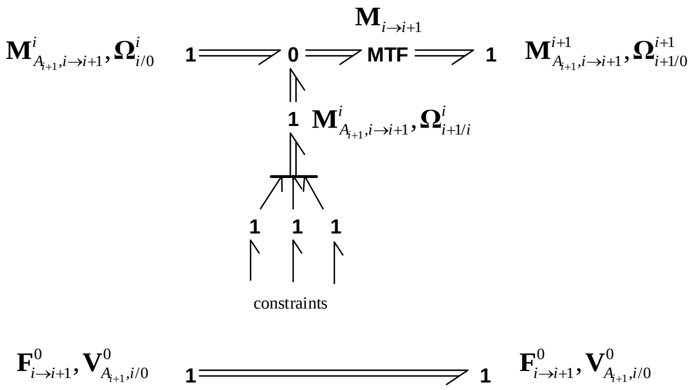

Figure 2-6. Multibond graph structure of a revolute or spherical joint

Revolute and spherical joints constrain all translational degrees of freedom, as a result the forces and velocities (in translation) that enter the joint are the same ones that leave the joint. In the upper part of the multibond graph on Figure 2-6 a zero junction is added to release the constraint on one angular velocity for a revolute joint or on three angular velocities for a spherical joint. In this last case, since no constraints would be enforced, the scalar bond graph one junctions would be just free. In the case of the revolute joint, the natural method to enforce two angular velocity constraints (e.g. around $\mathbf{X}_i$ and $\mathbf{Y}_i$) is to use null sources of flow, see case (a) of Figure 2-7. The consequence of this choice is that automatically after attributing causality (see Appendix 1), the inertial element that stores energy in rotation motion in body *i+1* will be in derivative causality (Van Dijk & Breedveld, 1991), (Tod, Malburet, Gomand, & Barre, 2013), which means that the underlying mathematical model becomes a Differential Algebraic Equations (DAE). Numerical simulations of the model can still be performed with adapted numerical methods (Van Dijk & Breedveld, 1991). Two methods have been proposed (Van Dijk & Breedveld, 1991) to remove derivative causalities that can be applied to joints. The first one consists in replacing the null sources of flow by high stiffnesses and dampers, sometimes called parasitic elements (Van Dijk & Breedveld, 1991). This method removes the derivative causality on inertial elements but the underlying mathematical model will be 'stiff' Ordinary Differential Equations (Van Dijk & Breedveld, 1991) and also has the disadvantage to introduce new state variables and therefore new modes that will perturb the analysis of the system. In addition, there is no systematic method to choose the value of stiffness and damping of these elements; however identified to actual components physical stiffness & damping characteristics. The last method consists in enforcing constraints by Lagrange multipliers (Borutzky, 2009), (Van Dijk &

Breedveld, 1991), which removes the derivative causality but the underlying mathematical model is this time composed of DAEs of index[12] 2 (Van Dijk & Breedveld, 1991), (Borutzky, 2009).

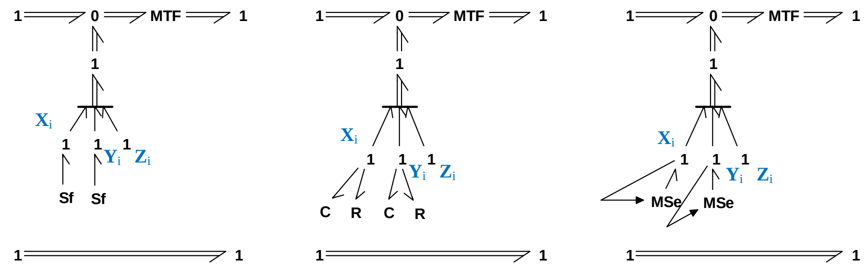

(a). null velocities constraint (b). parasitic elements (c). Lagrange multipliers

Figure 2-7. Three methods to implement joint constraints

A comparison between the three methods and others is proposed on a simple physical system in (Van Dijk & Breedveld, 1991) and the conclusion is that even if the three implementations can be solved by a BDF numerical method, the Lagrange multiplier method *"results are less accurate and the computational effort is higher in comparison to the case where causal paths between inertia ports are accepted and a DAE system of index 1 is solved*" (Borutzky, 2009) about (Van Dijk & Breedveld, 1991).

This section has discussed on how to model a multibody system of rigid bodies using Newton-Euler equations in bond graphs and how to implement constraints using joints. Finally it was shown how the implementation of constraints in joints might lead to a specific mathematical model which is in the general case a DAE system of varying index.

In our application the previously presented modeling method is applied to model the rotor-airframe system which consists in one rigid body for the fuselage and four rigid bodies for the rotor blades. A revolute joint between the airframe and the hub is implemented. Each blade is then attached to the hub through the concatenation of three revolute joints in the following order: first for the lag motion, then flap and finally pitch, see Figure 2-3. A contribution to the modeling of this concatenation is proposed, in the next paragraph that suppresses equation constraints at the graphical level.

---

[12] Index: number of times the constraint equation has to be differentiated to obtain a system of ODEs (Van Dijk & Breedveld, Simulation of system models containing zero-order causal paths—I. Classification of zero-order causal paths, 1991)

2.1.2. Joint between blade and hub for lag-flap-pitch motions

The proposed representation could be classified with the classic methods of reduction of equations of motion such as transformation of inertial bond graph elements (Van Dijk & Breedveld, 1991), (Borutzky, 2009). This representation has been presented at the iNacomm 2013 conference at the Indian Institute of Technology, Roorkee, see (Tod, Malburet, Gomand, & Barre, 2013).

By attaching the reference frame 4 to the hub, see Figure 2-8 and Figure 2-3, each blade angular velocity is defined as follows,

$$\mathbf{\Omega}_{blade/hub} = \dot{\delta}\mathbf{z}_4 + \dot{\beta}\mathbf{x}_\delta + \dot{\theta}\mathbf{y}_\beta \tag{17}$$

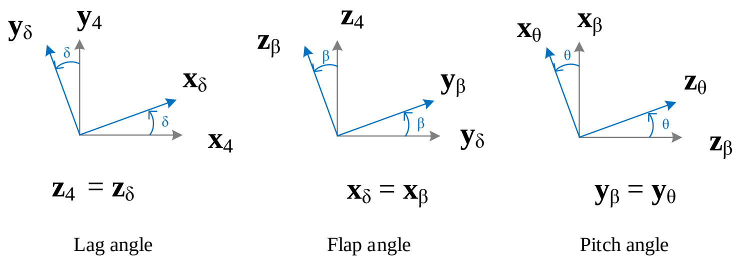

Figure 2-8. Individual blade angle definitions

On Figure 2-9, the concatenation of three revolute joints that represent equation (17) are presented with a ‘classic’ structure (a) and the proposed structure without the inclusion of any null sources of flow to relax causality (Tod, Malburet, Gomand, & Barre, 2013).

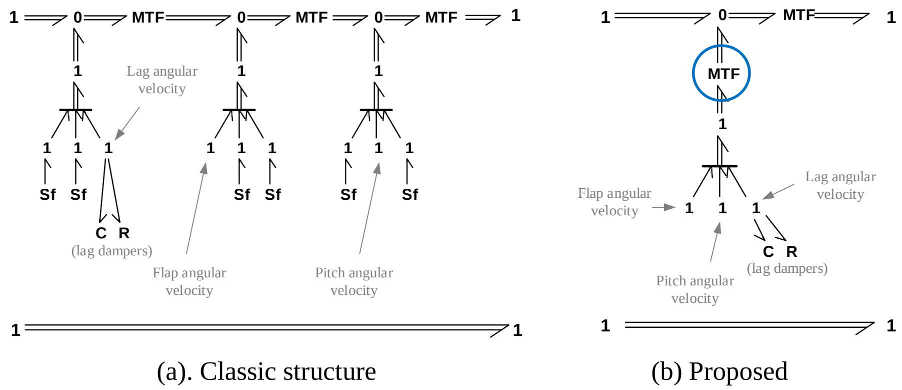

Figure 2-9. Concatenation of three revolute joints proposal

The use of the proposed structure demands to introduce a modulated multiport transformer element (circled in blue on Figure 2-9) which contains a matrix that has to be derived by projecting all the vectors of the equation (17) in the reference frame 4 (hub). It leads to the matrix below, which is a rotation matrix from a non-orthogonal frame to an orthogonal one,

$$\mathbf{M}_{x_\delta, y_\beta, z_4 \to hub} = \begin{bmatrix} \cos\delta & -\cos\beta\sin\delta & 0 \\ \sin\delta & \cos\beta\cos\delta & 0 \\ 0 & \sin\beta & 1 \end{bmatrix} \tag{18}$$

$$\mathbf{\Omega}^{hub}_{blade/hub} = \mathbf{M}_{x_\delta, y_\beta, z_4 \to hub} \begin{pmatrix} \dot{\beta} \\ \dot{\theta} \\ \dot{\delta} \end{pmatrix} \tag{19}$$

$$\mathbf{MTF} = \begin{bmatrix} 0 & \mathbf{M}_{x_\delta, y_\beta, z_4 \to hub}{}^{T} \\ \mathbf{M}_{x_\delta, y_\beta, z_4 \to hub} & 0 \end{bmatrix} \tag{20}$$

It has been verified analytically in (Tod, Malburet, Gomand, & Barre, 2013) that the proposed structure is also dynamically equivalent to the classic one and illustrated by the simulation of an inertial navigation system. In that example, the proposal allowed to obtain to an ODE system of equations of motion instead of a DAE system improving the computational efficiency. It should be noticed that the proposed rotation matrix is not always invertible for particular angles but that this could be overcome by redeveloping the idea using other definitions for the angles such as quaternions. In our application, angles will not vary more than +/-10° for which this matrix is not singular. Finally the kinematic relation at the zero junction of the proposed joint is simply,

$$\mathbf{\Omega}^{hub}_{hub/0} + \mathbf{\Omega}^{hub}_{blade/hub} = \mathbf{\Omega}^{hub}_{blade/0} \tag{21}$$

As a result the non-circled modulated multiport transformer element of the proposal in Figure 2-9 transforms vectors from the hub reference frame to the blade reference frame,

$$\mathbf{MTF} = \begin{bmatrix} 0 & \mathbf{M}_{hub \to blade}{}^{T} \\ \mathbf{M}_{hub \to blade} & 0 \end{bmatrix} \tag{22}$$

With,

$$\mathbf{M}_{hub\to blade} = \mathbf{M}_{R_\beta \to blade}.\mathbf{M}_{R_\delta \to R_\beta}.\mathbf{M}_{hub\to R_\delta}$$
$$= \begin{bmatrix} \cos\theta & 0 & \sin\theta \\ 0 & 1 & 0 \\ -\sin\theta & 0 & \cos\theta \end{bmatrix}^T . \begin{bmatrix} 1 & 0 & 0 \\ 0 & \cos\beta & -\sin\beta \\ 0 & \sin\beta & \cos\beta \end{bmatrix}^T . \begin{bmatrix} \cos\delta & -\sin\delta & 0 \\ \sin\delta & \cos\delta & 0 \\ 0 & 0 & 1 \end{bmatrix}^T$$

2.1.3. Quasi-steady aerodynamic forces

The previous sections have justified the modeling of the rotor-airframe system. In this section, the modeling of quasi-steady aerodynamic forces applied to each rotor blade is proposed.

Aerodynamic forces play a fundamental role; however their modeling is an ongoing research challenge by itself. More sophisticated approaches include unsteady aerodynamics, stall and free wake geometry models. The aerodynamic forces can be considered in a first approach in the investigation of low frequency phenomena by considering the lifting-line theory with quasi-steady aerodynamics (Bielawa, 2006). In (Dryfoos, Kothmann, & Mayo, 1999) inflow velocity is neglected since the inflow dynamics are expected to be generally faster than the dynamics of interest. In the same paper it is argued that it can be reasonably well approximated by replacing the Lock number with the reduced Lock number: usually between 60 to 70% of the actual Lock number.

Since the bodies represented before are considered as rigid for the dynamics of our interest, there is no need to any spatial discretization in the modeling. However, if flexible bodies where to be modeled, a spatial discretization would have been necessary for which bond graph representations exist (Borutzky, 2009). When modeling a blade, it can be necessary also to take into account for the variable characteristics (such as lift coefficient) of blade sections along their spans. In this case, a discretization of the velocity field along the blade span is necessary. The proposed modeling serves this potential need and has also the advantage leaving the possibility to represent not only hover flight but also forward flight configurations without any aerodynamic model modification.

By considering the point M of a blade section, the local lift force $\mathbf{dF}_{\text{air}\rightarrow\text{blade}}$, blade pitch angle θ_i, and section incidence angle *i*, inflow angle Φ and velocity $\mathbf{v}_{\text{air/blade}}$ see Figure 2-10.

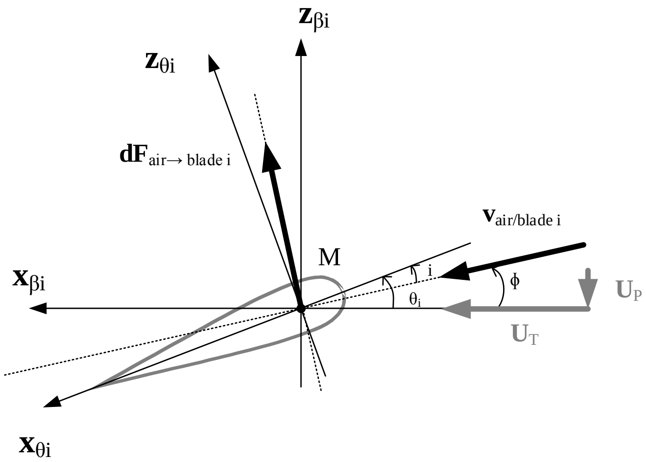

Figure 2-10. Quasi-steady aerodynamics model – per section

The expression of the local lift force is,

$$dF_{air\rightarrow blade} = \frac{1}{2}\rho c C_L \mathbf{v}^2_{air\rightarrow blade} dr \tag{23}$$

Where without considering the inflow velocity and no airframe advancing velocity,

$$\begin{aligned} \mathbf{v}_{air/blade} &= \underbrace{\mathbf{v}_{air/0}}_{=0} - \mathbf{v}_{blade/0} \\ &= \mathbf{U}_P + \mathbf{U}_T \\ &\approx \mathbf{U}_T \end{aligned} \tag{24}$$

Therefore,

$$\begin{aligned} \mathbf{U}_P &= -\mathbf{v}_{blade/0}.\mathbf{x}_\beta \\ \mathbf{U}_T &= -\mathbf{v}_{blade/0}.\mathbf{z}_\beta \end{aligned} \tag{25}$$

And assuming small incidence angles and small pitch angles,

$$\begin{aligned} i = \theta - \phi &= \theta - \arctan\frac{U_P}{U_T} \\ &\approx \theta - \frac{U_P}{U_T} \end{aligned} \tag{26}$$

The lift coefficient can then be expressed by,

$$C_L = \frac{\partial C_L}{\partial i}.i \approx c_l.i \tag{27}$$

Which leads to the following aerodynamic force expression,

$$dF_{air\to blade} = \frac{1}{2}\rho c c_l \left(\theta U_T{}^2 - U_P U_T\right) dr \tag{28}$$

And by introducing the Lock number γ, which represents the ratio between aerodynamic and inertia forces,

$$\gamma = \rho \frac{c.c_l}{I_{bl}} R^4 \tag{29}$$

$$dF_{air\to blade} = \frac{\gamma I_{bl}}{2R^4}\left(\theta U_T{}^2 - U_P U_T\right) dr \tag{30}$$

The expression of the lift force on the blade would be,

$$F_{air\to blade} = \int_0^R dF_{air\to blade} \tag{31}$$

The integral can then be approximated using the rectangle method,

$$\int_0^R dF_{air\to blade} = \lim_{n\to+\infty} \frac{R}{n}\sum_{k=0}^{n-1} \frac{dF_{air\to blade}}{dr}(k) \tag{32}$$

This finally becomes, for *n* large enough,

$$\int_0^R dF_{air\to blade} \approx \frac{R}{n}\sum_{k=0}^{n-1} \frac{dF_{air\to blade}}{dr}(k) \tag{33}$$

With,

$$\frac{dF_{air\to blade}}{dr}(k) = \frac{\gamma(k) I_{bl}}{2R^4}\left(\theta U_T(k)^2 - U_P(k) U_T(k)\right) \tag{34}$$

Finally, the moment of the forces can be expressed analytically at the blade root A,

$$\int_0^R \mathbf{AM} \wedge \mathbf{dF}_{air\to blade} \approx \frac{R}{n}\sum_{k=0}^{n-1} \mathbf{AM}_k \wedge \frac{d\mathbf{F}_{air\to blade}}{dr}(k) \tag{35}$$

By the way the multibond graph of a rigid body was generated, see Figure 2-5, the previous moment has to be expressed not at the blade root A but around the center of mass of the blade. This leads to a multibond graph representation that has *n* branches for which only the k^{th} one has been represented; the two horizontal bonds, see Figure 2-11, transport the power input from the blade multibond graph, see Figure 2-5.

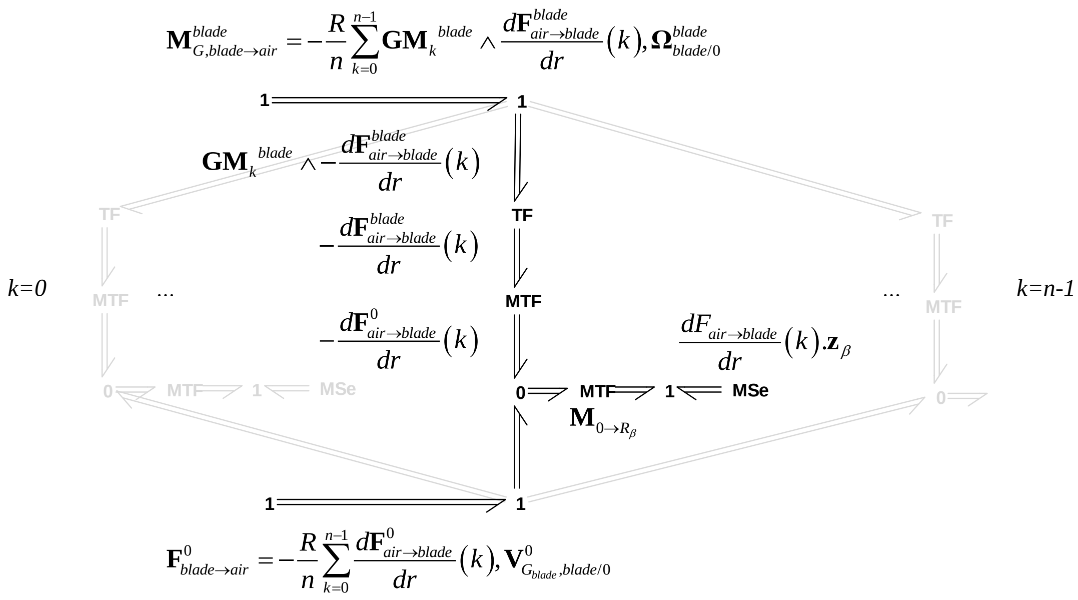

Figure 2-11. A flexible model to represent quasi-steady aerodynamic forces by spatial discretization of the blade velocity field along its span

2.2. Aeromechanical model validity

In this section, the validity of the rotorcraft model constructed previously is discussed in three steps. First, a rotor, with flapping blades including aerodynamic forces, attached to the ground is verified against the classic flapping equation (36). Then this rotor is attached to a rigid body fuselage with one vertical degree of freedom and compared with an identification experiment lead at Airbus Helicopters. Finally, the lateral and roll degrees of freedom of the fuselage are released as well as the lag degree of freedom of each blade and compared to an equivalent model developed using Lagrange equations.
A general overview of the complete model is presented on Figure 2-15. The rotor subsystem contains the blades rigid bodies as well as the joints that constrain them to the hub, Figure 2-9. The model is implemented in a software that is able to represent both bond and multibond graphs such as 20-sim®.
The last point of importance in rotorcraft dynamics is the flight configuration. As a matter of fact, the flight configuration determines not only the equilibrium position around which dynamic phenomena may appear but it has also an impact on the system characteristics. For example, an important role is played by the aerodynamic damping in rotor stability; during forward flight the speed of advancing blades will be higher than retreating ones, leading to more aerodynamic damping on advancing blades; this is not the case in hover flight. Linearity around hover flight is justified by (Aponso, Johnston, Johnson, & Magdaleno, 1994), in which a helicopter dynamics linear model is developed and compared to flight tests of Sikorsky's CH-53E in hover; the results show a good agreement between the model and the tests for a range of frequencies between 1 and 10Hz.

The ground subsystem is a joint between the airframe and the inertial reference frame in which the first to the sixth degrees of freedom of the airframe can be blocked or released see Figure 2-12 by implementing constraints as explained in previous sections.

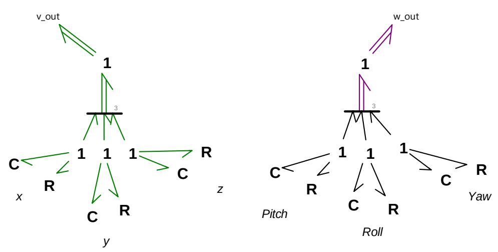

Figure 2-12. Ground subsystem

The engine subsystem contains only a source of flow that feeds the rotor angular velocity into the $\mathbf{z}_3$ axis (on Figure 2-3) of the revolute joint. The hub subsystem, Figure 2-13 has the multibond graph structure of rigid body in spatial motion described in Figure 2-5 from which inertial elements have been removed, since its mass and inertia are neglected; the dynamics of the hub and mast are therefore neglected but it could be interesting to include them in a more detailed study. It leaves to this structure mainly a kinematic role. The four branches to the right correspond to the power transmission bonds to the blades.

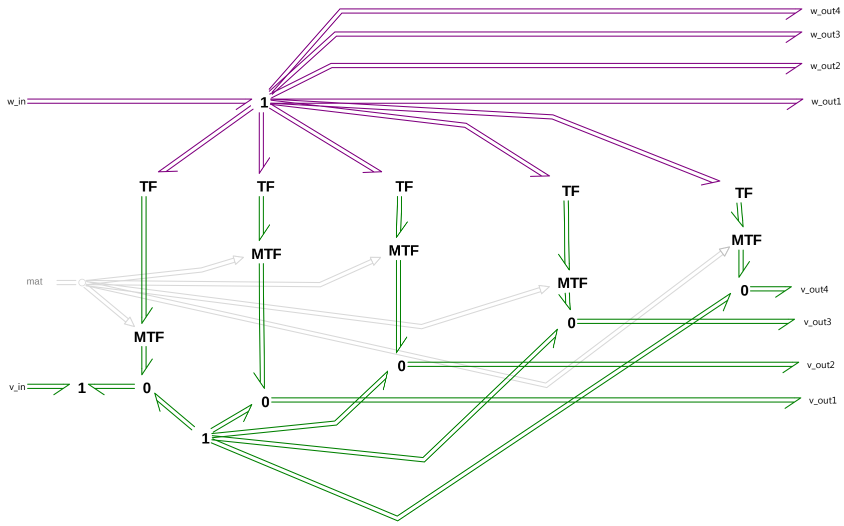

Figure 2-13. Hub subsystem and power outputs to blades

Concerning the controls subsystem, it has the structure presented on Figure 2-14, where all the gray elements are information bonds as they would appear in the software interface where the graph has been implemented and not transmit any power. The expression of the pitch transmitted to each blade via the bond graph sources of flow is also detailed on Figure 2-14.

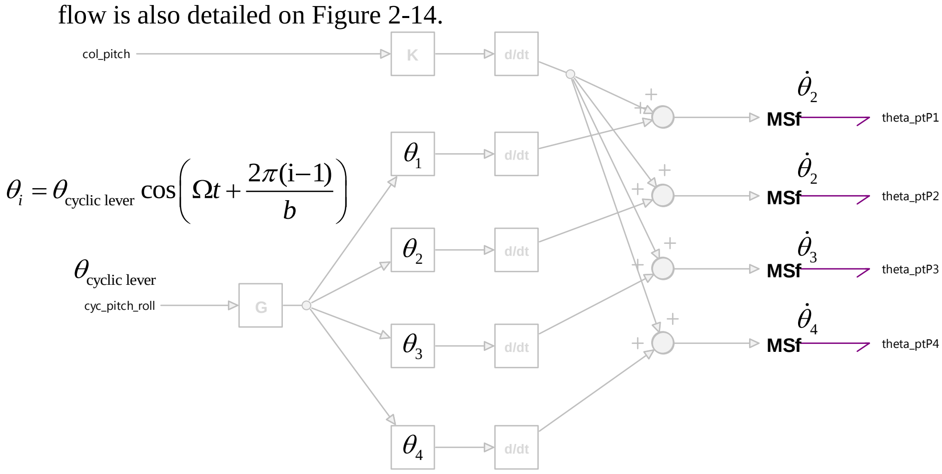

Figure 2-14. Controls subsystem

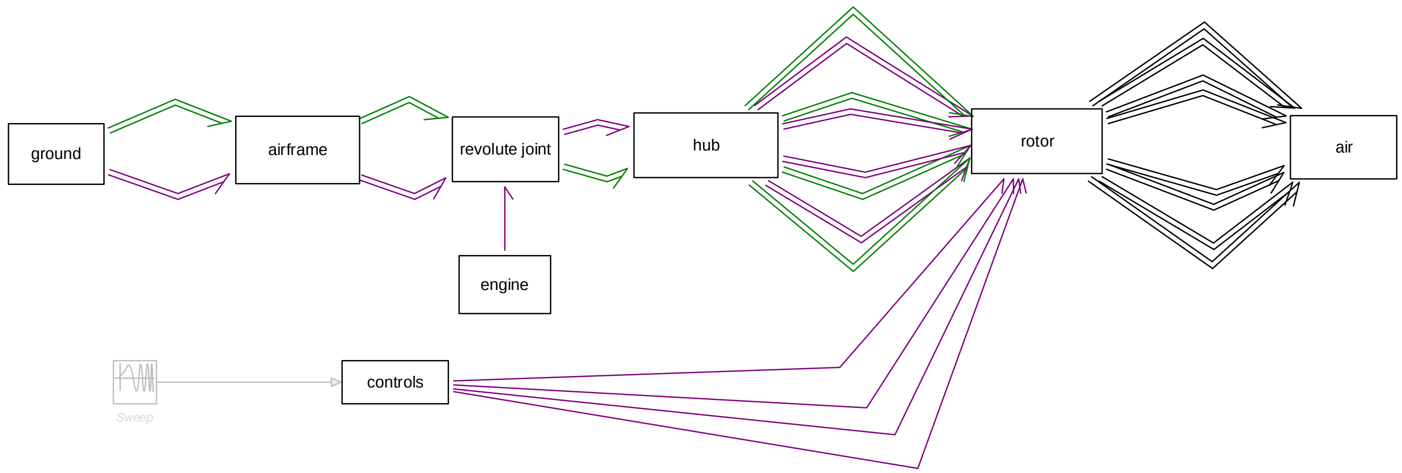

Figure 2-15. Rotorcraft system model using bond graphs

2.2.1. Rotor flapping dynamics

A very first step prior to the validation of the model is to verify whether the proposed aerodynamic forces model converges when the number of blade sections is higher. Very pragmatically, the model is proposed to be compared to the very classic flap equation of a rigid blade (Krysinski & Malburet, 2011),

$$I_{bl}\ddot{\beta}_i + \frac{I_{bl}\gamma\Omega}{8}\dot{\beta}_i + (I_{bl} + em_s)\Omega^2\beta_i = \frac{I_{bl}\gamma\Omega}{8}\theta_i \tag{36}$$

Where it can be seen that *e*, the blade hinge eccentricity, see Figure 2-3, shifts the flapping natural frequency from being the rotor angular velocity. Furthermore, the second term, which corresponds to a damping term takes its origin from aerodynamic forces, see equation (30). The right member of the equation contains the first part of aerodynamic forces which are proportional the blade pitch angle. This equation can be represented in a very compact form in a bond graph, Figure 2-16, that it is implemented next to the model Figure 2-15 for a comparative identification by numerical simulations under the same conditions.

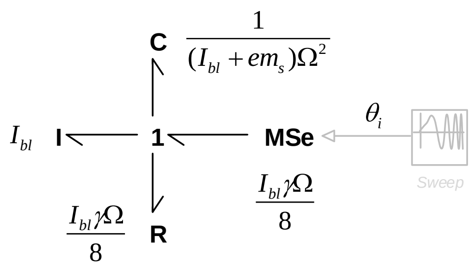

Figure 2-16. Flapping equation using bond graphs

Table 1. Rotor data

Rotor		
Number of blades	b	4
Radius	R (m)	7.5
Blade root eccentricity	e (m)	0.3
Lock number	γ	9
Angular velocity	Ω (rad/s)	29
Individual blade		
Static moment	m_s (m.kg)	390
Inertia	I_{bl} (m^2.kg)	1953

The isolation of the rotor multibody model is obtained by blocking the airframe degrees of freedom and blade lag motion. The forced flapping response of a blade is simulated numerically by sweeping the collective lever angle from 0 to 12 Hz and the results in the time domain are then plotted in the frequency domain using a discrete

Fourier transform, Figure 2-17. With this figure, it can be verified that the proposed modeling of quasi-steady aerodynamics converges with the increase of the number of elements and that it also converges to the linear equation especially below and after the natural flapping frequency.

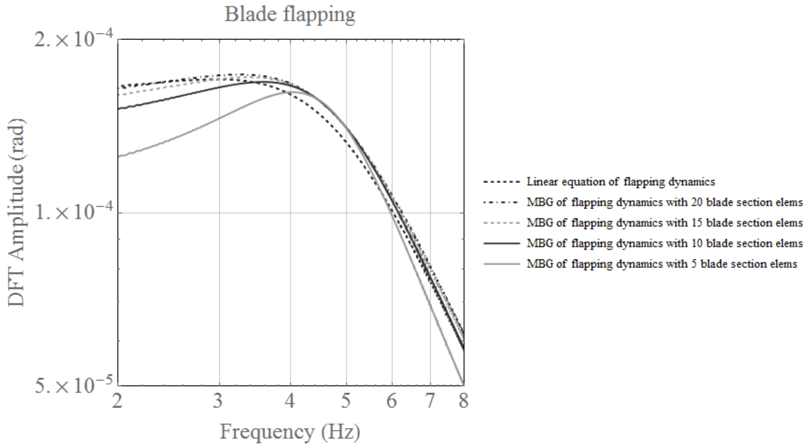

Figure 2-17. Identification of blade flapping response to collective pitch inputs

Around the natural frequency, the damping difference is due to a different approximation between the two models: in the multibond graph model there is no linearization on the calculation of the inflow angle *Φ*, see Figure 2-10 and equation (26). This is possible in the bond graph model because the velocities of the blade are available very naturally in the graph – however this is not a bond graph property and could have also been done from analytical equations solved numerically.

Table 2. Rotor static lift force numerical simulation from the bond graph model

$$F_{\text{static lift from rotor}} = b\int_{r=e}^{r=R} \frac{\gamma I_{bl}}{2R^4}\theta_i.\left(e\Omega + r\Omega cos(\beta_{0ss})\right)^2.dr$$

After numerical application, F=25 772 N

# of blade sections	Force(N)	Difference
20	22 200	13.8%
15	21 600	16.2%
10	20 550	20.3%
5	17 400	32.5%

In the end, from Table 2, it appears that the rotor static lift force converges when the number of blade sections is higher. The flapping dynamic behavior also converges with the number of elements, see Figure 2-17. Even if this verification might seem basic, it allows to verify that the 80 multi bonds of the aerodynamic model are well connected and paves the road towards more complex verifications.

2.2.2. Vertical dynamics validity on the ground

In this section, the previous model is modified: the vertical degree of freedom of the airframe is released. Then, pilot and flight control system dynamics models are inserted. A collective pitch sweep is used as an input and the behavior of the airframe is identified. This numerical experiment was compared (Orlita, 2015) to a real ground test performed at Airbus Helicopters.
The experiment performed at Airbus Helicopters on an actual helicopter. It consisted in measuring the vertical absolute accelerations of two components: the airframe and the collective lever, see Figure 2-18.

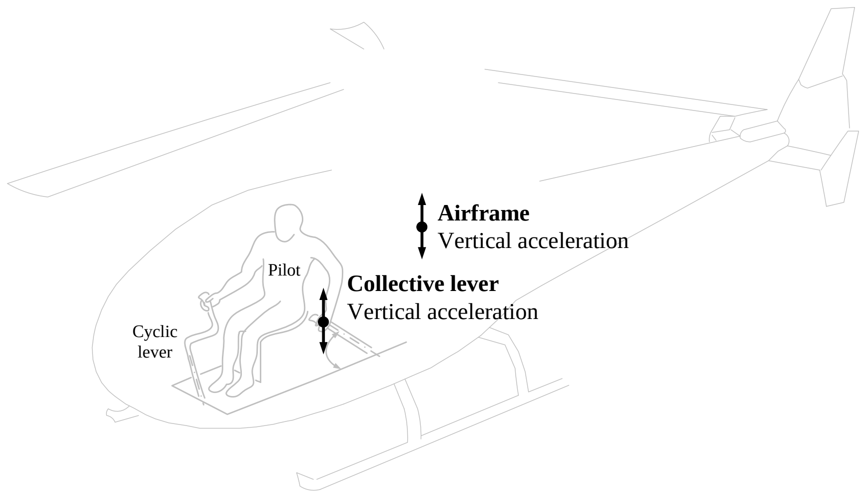

Figure 2-18. Acceleration measurements on the vertical axis during ground testing

The rotor angular velocity was close to nominal speed allowing the blades to flap as described in the previous section. In order to excite the system, the pilot was asked to apply a voluntary motion on the collective lever between 2 and 5Hz. The identification results of the collective lever to fuselage absolute accelerations are plotted in the frequency domain on Figure 2-19 (dashed green). A resonant frequency between 2 and 3Hz appears corresponding to the vertical mode of coupled rotor-airframe system while on the ground. The model proposed in Figure 2-15 of the previous section has been modified by closing the loop between the airframe and rotor collective pitch inputs see Figure 2-21 with a pilot and collective control subsystem. This subsystem contains a pilot model which is known in literature as Mayo's model (Mayo, 1989), that is the result of identifications of pilot behavior performed on one of Sikorsky's motion based simulators. It has been widely used in literature to investigate the vertical collective bounce phenomenon.

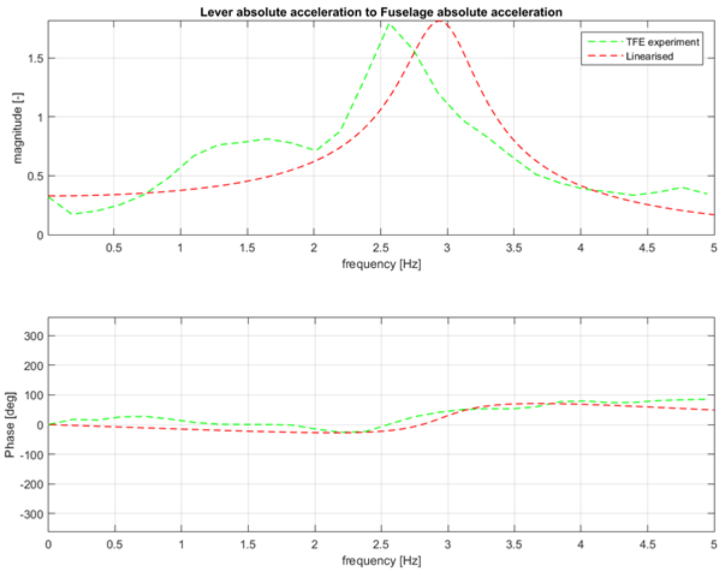

Figure 2-19. Experiment and numerical identification results of helicopter[13] vertical dynamics

The control subsystem of Figure 2-14 is replaced by the one on Figure 2-20. It contains both the pilot transfer function and a transfer function associated to the dynamics of vertical the flight control system. The resulting model has allowed obtaining the red dashed transfer function between the lever and airframe absolute accelerations on Figure 2-19.

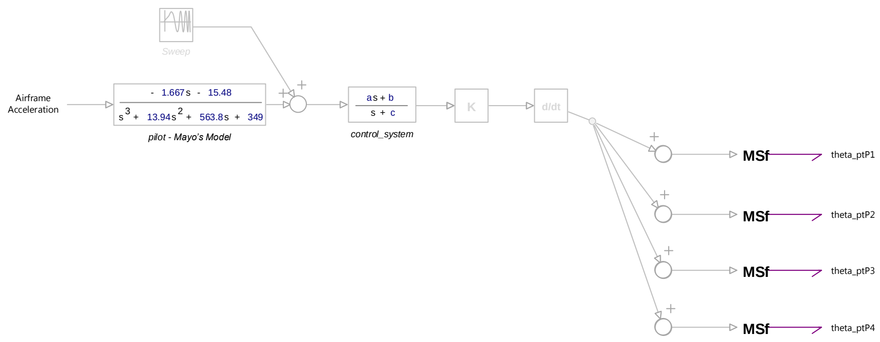

Figure 2-20. Pilot and control system subsystem model

---

[13] Without any scientific impact on the explanations, magnitudes have been intentionally deformed from actual measurements; helicopter details are intentionally not provided

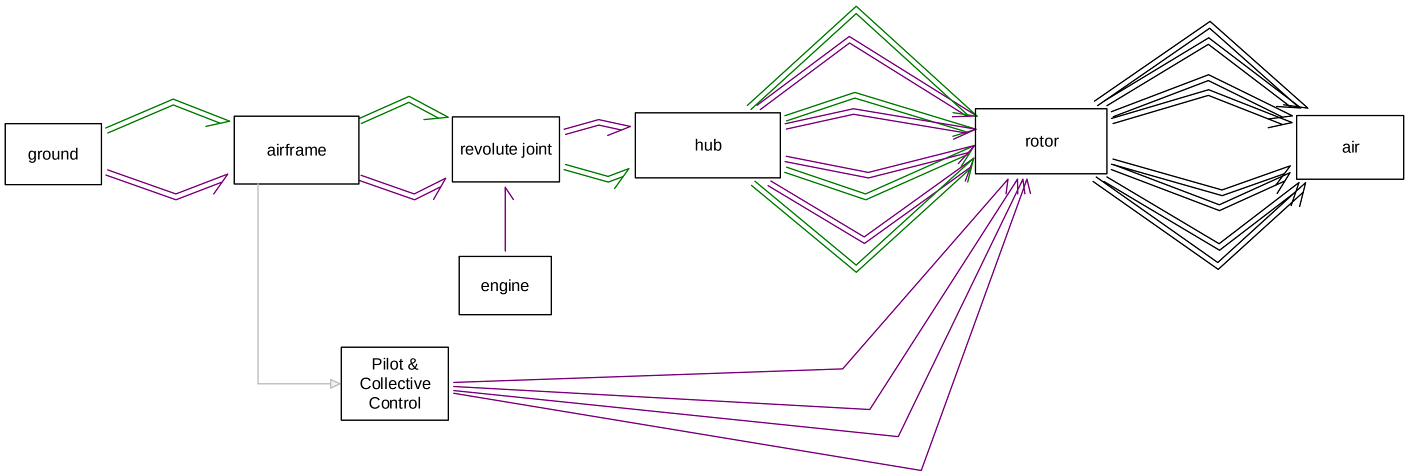

Figure 2-21. Closing the loop with pilot and collective control models for experimental confrontation

The model correlation with the experiment is quite satisfactory. Sensitivity analysis on pilot model parameters has shown this transfer function is pilot independent. Therefore it allows identifying the vehicle dynamics on the vertical direction.
The complete resulting bioaeroelastic model could help performing parametric sweeps of design variables of a given helicopter to investigate its proneness to 'vertical collective bounce', (Mayo, 1989), (Masarati & Quaranta, 2014), (Muscarello, Quaranta, & Masarati, 2014), (Orlita, 2015). However, it is preferred to focus on lateral-roll axes phenomena since less investigations are available in open literature.

2.2.3. Lateral/roll dynamics validity of the model around hover

In the two previous sections, the model has been 'downgraded' to verify the flapping dynamics of the rotor alone and illustrating how the aerodynamic model performs. Secondly the airframe was released on its vertical axis only and compared to an experiment performed on a real helicopter at Airbus Helicopters flight testing facility in which the results are quite encouraging. Ideally, the remaining axis of the model that have not been verified, namely lateral and roll dynamics of the helicopter should be compared to flight tests. However, being able to find flight test results can be as challenging as learning the bond graph language. As a result, a model has been developed using Lagrange equations based on the same hypothesis, see Rotor-airframe model using multibody dynamics section, Figure 2-2. Airframe axis definitions and Figure 2-3. Rotor i^{th} blade axis definitions. Both the bond graph multibody model and the analytical model developed using Lagrange equations can be derived from Hamilton's principle; as a result by verifying that both models match is expected to be a mutual verification of their physical validity. Of course this verification does not replace necessary experimental validations to be done in the future.

The principal steps of the development of the model using Lagrange equations are described so the hypothesis can be reviewed and the state-space resulting system is presented in Appendix 2. In this section the main focus will be on the modal analysis and time simulations of the resulting system and how it was compared with the bond graph model. The equations of motion are first linearized around hover flight, at this stage the resulting system is time-periodic and the multiblade coordinate transformation (Appendix 2) is used to obtain a time-invariant system that is put into state-space form Appendix 2.

A set of parameters is fixed for the helicopter and the pilot, see Table 3. These parameters correspond to a medium weight helicopter; the individual blade lag motion natural frequency ω_δ is inferior to the rotor angular velocity,

$$\omega_\delta = \sqrt{\frac{k_\delta}{I_{bl}}} = 1.53\ Hz\ \left(\approx 0.33\Omega\right)$$

The positioning of ω_δ corresponds to a soft-in-plane rotor technology ($\omega_\delta < \Omega$) and has lightly damped in-plane rotor modes see Figure 2-22.

Table 3. Helicopter data

Main rotor		
Number of blades	b	4
Radius	R (m)	7.5
Blade root eccentricity	e (m)	0.3
Lock number	γ	9
Angular velocity	Ω (rad/s)	29
Steady-state coning angle	β_{0ss} (rad)	0.0175
Individual blade		
Static moment	m_s (m.kg)	360
Inertia	I_{bl} (m².kg)	1728
Mass	M_{bl} (kg)	100
Equivalent angular lag damper stiffness	k_δ (N.m/rad)	160000
Equivalent angular lag damper damping	c_δ (N.m.s/rad)	3000
Airframe		
Mass	M_f (kg)	7500
Roll inertia around center of mass	I_{yy} (kg)	10000
Rotor head height from center of mass	h (m)	2
Cyclic blade pitch/lever roll angle		
Gearing ratio	G	0.1

A modal analysis of the system is conducted and shows the classic repartition of regressing, advancing lag and flap modes in the complex plane, see Figure 2-22, as it can be found in literature (Takahashi & Friedmann, 1991).

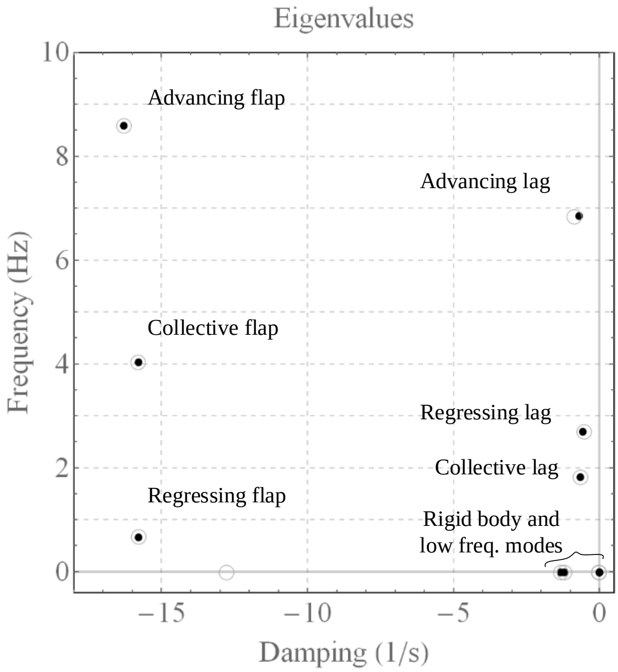

Figure 2-22. Eigenvalues without (•) and with (○) extra stiffness and damping terms

A pure lateral static mode appears in the system as unstable. This mode is not physical, it appears due to the reductive modeling hypothesis; at low frequencies, one would expect *Dutch roll* eventually, see Figure 1-8. In order to perform a time simulation of the system of equations resulting from the nonlinear bond graph model, this mode has to become stable. Very interestingly, this mode disappears once the pilot model will be included.
To stabilize the mode, stiffness and damping terms are added to the lateral and roll degrees of freedom ($kp_x=0.1N/m$, $kd_x=1.10^5N.s/m$, $kp_{\alpha y}=0.10.1N.m/rad$, $kd_{\alpha y}=0.1\ N.m.s/rad$) in both analytical and bond graph model resulting in the modal analysis of empty circle on Figure 2-22 and on stabilization of the lateral airframe static mode see Figure 2-23.

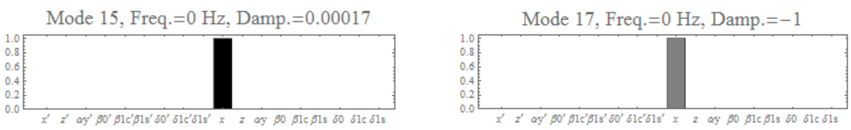

(a). without, unstable mode

(a). with, stable mode

Figure 2-23. Lateral airframe static mode shape without and with extra stiffness and damping terms

It should be noticed that most modes are not affected by this additional terms, see Appendix 3.

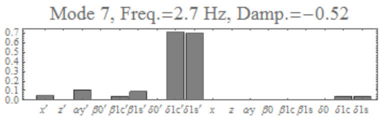

(a). regressing lag mode

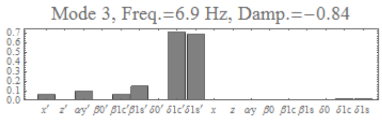

(a). advancing lag mode

Figure 2-24. Weakly damped modes

The linear equations of motion are presented on Appendix 2: a closer look at the equation on the vertical axis, see (A2.2), shows that with the chosen hypothesis the vertical motion is uncoupled from flapping and lagging cyclic motion. It is therefore chosen to block the vertical axis translation of the airframe on the bond graph. Once this is done, the forced response of the stable system Figure 2-15 to swept inputs of roll cyclic pitch inputs Figure 2-25 is simulated from both bond graph and analytical models.

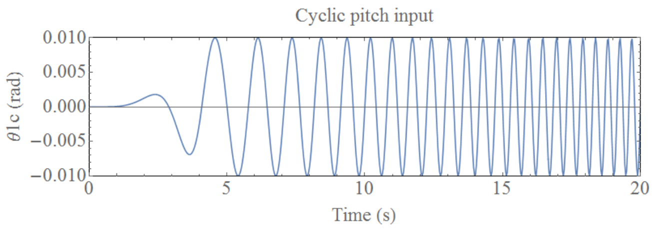

Figure 2-25. Roll cyclic pitch input sweep between 0 and 10 Hz in 100s (only first 20s plotted)

On Figure 2-26, the first two columns are the time simulation results from respectively linear and nonlinear (from the bond graph Figure 2-15) models. The last column presents discrete Fourier transforms of the first two columns results. For every state variable of that figure, the two peaks of both regressing and advancing lag modes are recognizable, see Figure 2-24. The scale is the same for all plots shows pretty good agreement, except at very low frequencies for the flapping response and in between peaks for the lateral airframe velocity; it is invoked here that it comes from a difference in the aerodynamic model using bond graphs that does not approximate the computation of the angle of attack see equation (26). It is interesting to remark that once the pilot model will be included, the parasitic elements that have been introduced here are not needed anymore to obtain a stable system that can be simulated numerically.

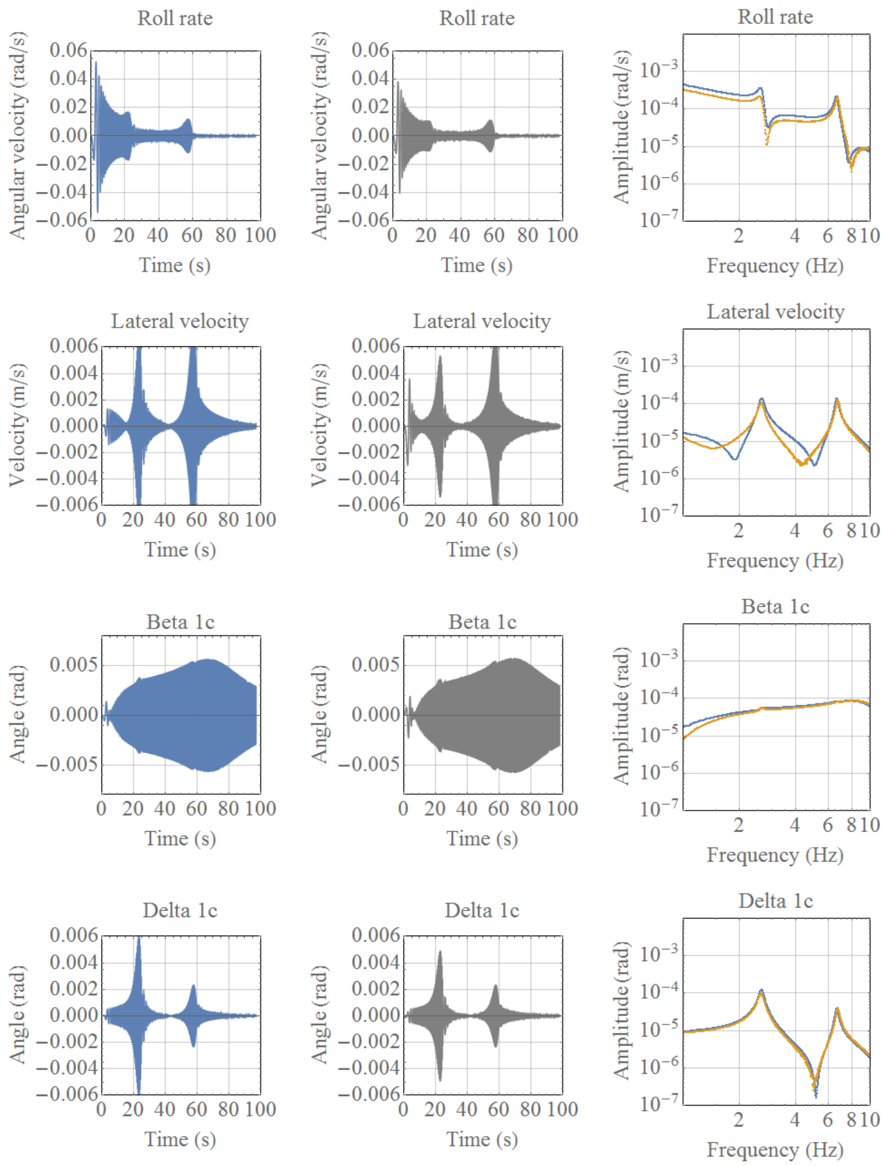

(a) Analytical

(b) Bond graph

(c) Analytical (blue)
Bond graph (orange)

Time simulations

Discrete Fourier Transforms

Figure 2-26. Identification of analytical and bond graph models forced responses of a helicopter around hover

2.3. Conclusion

In this chapter, the development of an aeromechanical rotor-airframe model is proposed to be representative of the real physical system at low frequencies. The quasi-steady aerodynamics forces graph is considered to be an original contribution. It both allows to take into account for variable aerodynamic properties along its span and can be used without any modification to represent hover or forward flight configurations. The model behavior has been compared to ground test results on the vertical axis for which it seems to be representative enough of what has been measured. On the lateral-roll axes of the airframe, the model has not been compared to flight tests since no data was available in the open literature. However, it has been compared to a linear model of the same assumptions but using Lagrange equations for which the agreement seems between the two is satisfactory.

The proposed model needs to be compared to flight tests to be considered as valid in the future. One of the first improvements that will need to be done on the modeling hypothesis concerns the necessity to take into account rotor inflow velocity in the aerodynamic model. The implementation of unsteady aerodynamic models should also be investigated. However, it should be kept in mind that bond graphs represent naturally *differential equations* and not *partial differential equations*. If the need is such, a more adapted energetic method could be used such as *Port-Hamiltonian Systems*, an evolution of bond graphs (Schaft, 2006).

Concerning the method, using the multibody system approach in bond graphs has of course the advantage of being applicable to a large class of problems but the drawback of probably not being the most computationally efficient for a particular problem. In fact, when modeled with such procedure, the equations of motion can be obtained relatively easily. However, as often in mechanics, the easier the equations of motion are obtained, the more complex the mathematical models are: not only Ordinary Differential Equations (ODEs) appear but also Differential Algebraic Equations (DAEs).

It has also been illustrated that in order to limit the number of DAEs, it is possible to act at the graphical level. In this work, most constraints were implemented using parasitic elements. It is a systematic method that can be used at the graphical level to remove the derivative causality on inertial elements of rigid bodies to limit the number of DAEs but the underlying mathematical model will after that include ‘stiff’ ODEs; it also has the disadvantage to introduce new state variables and therefore new modes that will perturb the analysis of the system.

When modeling the joint between each blade and hub of an articulated rotor, an original bond graph representation is proposed to avoid using parasitic elements or Lagrange multipliers. It consists in a local reduction of the equations that can be implemented at the graphical level in every system where three revolute joints need to be concatenated. The proposed representation could be classified with the classic methods of reduction of equations of motion such as transformation of inertial bond graph elements.

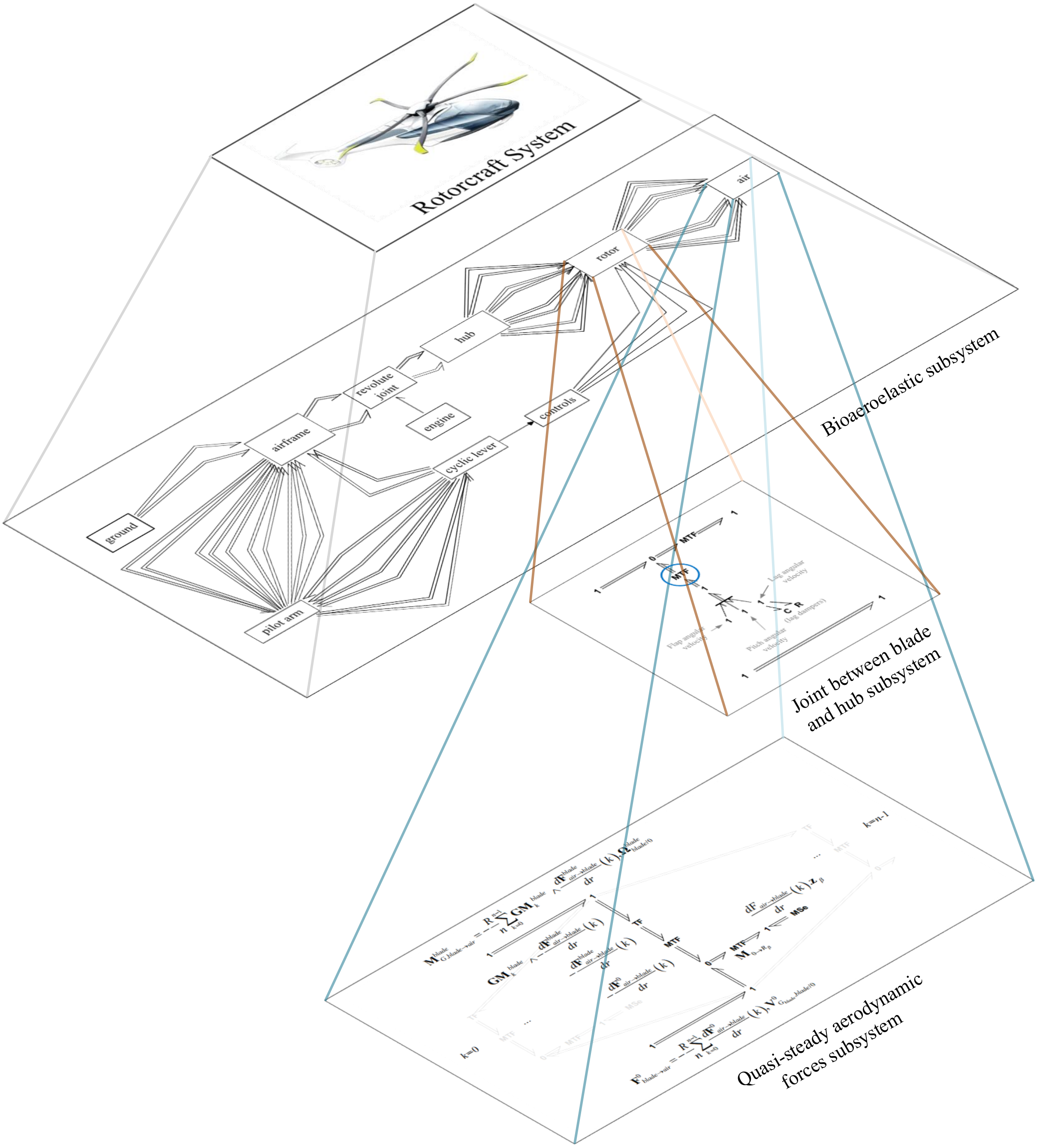

Figure 2-27. Chapter 2 main modeling blocks contribution to the global modeling approach